

OPEN

Versatile and High-throughput Force Measurement Platform for Dorsal Cell Mechanics

Seungman Park¹, Yoon Ki Joo² & Yun Chen^{1,3,4}

We present a high-throughput microfluidics technique facilitating *in situ* measurements of cell mechanics parameters at the dorsal side of the cell, including molecular binding strengths, local traction forces, and viscoelastic properties. By adjusting the flow rate, the force magnitude exerted on the cell can be modulated ranging from ~14 pN to 2 nN to perturb various force-dependent processes in cells. Time-lapse images were acquired to record events due to such perturbation. The values of various mechanical parameters are subsequently obtained by single particle tracking. Up to 50 events can be measured simultaneously in a single experiment. Integrating the microfluidic techniques with the analytic framework established in computational fluid dynamics, our method is physiologically relevant, reliable, economic and efficient.

Force measurement studies have quantitatively informed the interactions between binding partners at the molecular level, the orchestrated force-generating machinery such as cell migration and endocytosis, at the organelle level, and the mechanical properties of the cells at the cellular level^{1–3}. A host of techniques has been developed to serve these purposes depending on the length scale. For example, optical trap^{4,5}, atomic force microscopy (AFM)^{6,7}, DNA-based force sensors^{8–10}, are commonly used to measure the binding strength between two species of molecules; traction force microscopy (TFM)^{11,12} and microposts^{13,14} are commonly used to measure the contractile forces generated by cells; magnetic tweezers^{15,16} and micropipette aspiration^{17,18} are widely used to measure the viscoelastic properties of single cells. Most of the force measurement techniques described above are used in a narrow range of length scales, either at the molecular level, the organelle level or the cellular level. In addition, the techniques are low-throughput and can only measure one or a few test objects at a time. In particular, AFM and optical traps had been used to probe the mechanical properties of the cells, but their relatively low throughput capacity results in time-consuming measurements to survey sample populations to achieve statistical significance, especially in the case when there is high heterogeneity in the sample population. Here we developed a new microfluidic-based platform and corresponding technique, which is versatile to measure forces across multiple length scales. By computing the hydrodynamic forces based on the acquired images, our new technique can measure molecular binding strengths, local traction forces, and viscoelastic properties of the cell. Our technique is relatively low-cost compared to others, requiring a syringe pump and flow chambers (Fig. 1a). By adjusting the flow rate, the applied force magnitude can be modulated within a wide range, from approximately 14 pN to 2 nN (Fig. 1b), suitable for measuring many force-mediated processes. The experiments are recorded using time-lapse bright-field microscopy at low magnification (10X), which provides a large field of view, thus high-throughput readouts, measuring up to 50 events at a time.

Results and Discussion

We first set out to demonstrate that we could measure traction forces at the dorsal side of the cell. It should be noted that while there are multiple well-established methods to measure traction forces at the ventral side of the cell^{19,20}, including traction force microscopy (TFM) and micropost assays, few methods exist to measure dorsal traction forces²¹. However, dorsal traction forces are of biological importance as well. For example, dorsal traction forces are involved in disrupting cancer cell-endothelium association during intravasation^{22,23}, or in cell motility of neural crest during embryonic development^{24–26}, or during the interaction between the cancer cells and immune cells^{18,27–29} which might result in immunosuppression. Here we used our platform to examine the force

¹Department of Mechanical Engineering, Johns Hopkins University, Baltimore, MD, USA. ²Department of Chemical and Biomolecular Engineering, Johns Hopkins University, Baltimore, MD, USA. ³Center for Cell Dynamics, Johns Hopkins University, Baltimore, MD, USA. ⁴Institute for NanoBio Technology, Johns Hopkins University, Baltimore, MD, USA. Correspondence and requests for materials should be addressed to Y.C. (email: yun.chen@jhu.edu)

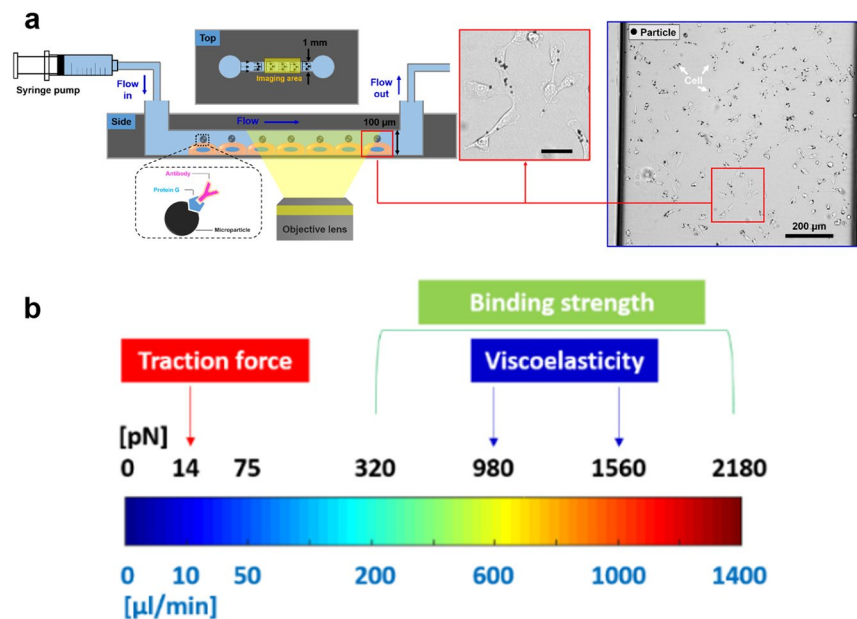


Figure 1. The traction force, viscoelastic properties, and bond strength of the dorsal side of cells were evaluated using the microfluidic device at high-throughput. (a) Cells are seeded in a microfluidic channel and then particles coated with ligand targeting surface molecules are added to bind to the cell surface. To induce hydrodynamic forces, a syringe pump and tubing are used. Particle-bound cells are shown in the inset marked (red box, Scale bar: 50 μm). Whole field of view of actual image taken for highthroughput analysis was shown (blue box). Black dots indicate particles attached to cells (white arrows). (b) Force spectrum is shown as a function of flow rate. Different flow rates can be applied for various types of measurement. For example, to measure the traction force, a force in the range of tens of pN is used. To measure the viscoelastic properties, forces of in the range of 1 nN are used. To measure the bond strength, a varied force which increases in a stepwise manner is used, ranging from ~ 300 pN to ~ 2000 pN.

transmitted to the key immunosuppressing molecule cytotoxic T-lymphocyte-associated protein 4 (CTLA4)^{30–34} on the surface of cancer cells. It has been reported CTLA4 was involved in mechanically engaging its ligands CD80 or CD86 leading to immunosuppression^{28,30,35,36}, though the magnitude of the mechanical forces transmitted via CTLA4 is yet to be quantified. We tracked the displacement of micron-sized particles conjugated with CD80, which bound to CTLA4³⁷ on the surface of breast cancer cells (MDA-MB-231). Based on the tracking results, we calculated the magnitude of the traction force generated by the cells to overcome the hydrodynamic forces and subsequently move the particle in the direction opposite to the flow. In our system, the bond between CD80 and CTLA4 was mechanically engaged when CD80-coated particles were subjected to low hydrodynamic forces at the flow rate of 10 $\mu\text{l}/\text{ml}$, the hydrodynamic forces provided by the flow forms strong catch bonds^{38,39}, enabling CTLA4 linked to the actomyosin machinery⁴⁰ to withstand the tension while being displaced opposite to the flow direction. Therefore, the traction forces were then transmitted effectively, evident by the observation of particles being displaced in the opposite direction to the flow (Supplementary Movie S1). It should be noted that without the low hydrodynamic forces supplied by the flow, the catch bond was not activated, and no traction forces between CD80 and CTLA4 could be detected (data not shown).

The traction forces were estimated using the equation

$$F_C = F_A + F_D \quad (1)$$

where F_C , F_A , and F_D are the traction force generated by cell, applied hydrodynamic force, and drag forces at the interface, respectively (Fig. 2a). To estimate the hydrodynamic forces caused by the flow, calculation based on the Stokes equation was used. Stokes equation is applicable to objects moving uniform flow under laminar flow⁴¹, and the maximum Reynolds number in all our experimental configurations are less than 40. In addition, when the particles move near the solid boundary, the wall effects should be taken into account^{41,42}. Therefore the applied hydrodynamic force exerted on particles was calculated using the modified Stokes equation^{41,43} (Materials and Methods, Supplementary Figs S1–S4 and Table S1):

$$F_A = 6\pi a\mu C \quad (2)$$

where a , μ , u , and C represent the particle radius, the dynamic viscosity of the medium, particle velocity and correction factor. Particle tracking results showed that the particles moved at constant velocity, indicating the particles experienced constant hydrodynamic force throughout the experiment. Since particles move near the channel surface, wall effects should be taken into account using the correction factor (C)

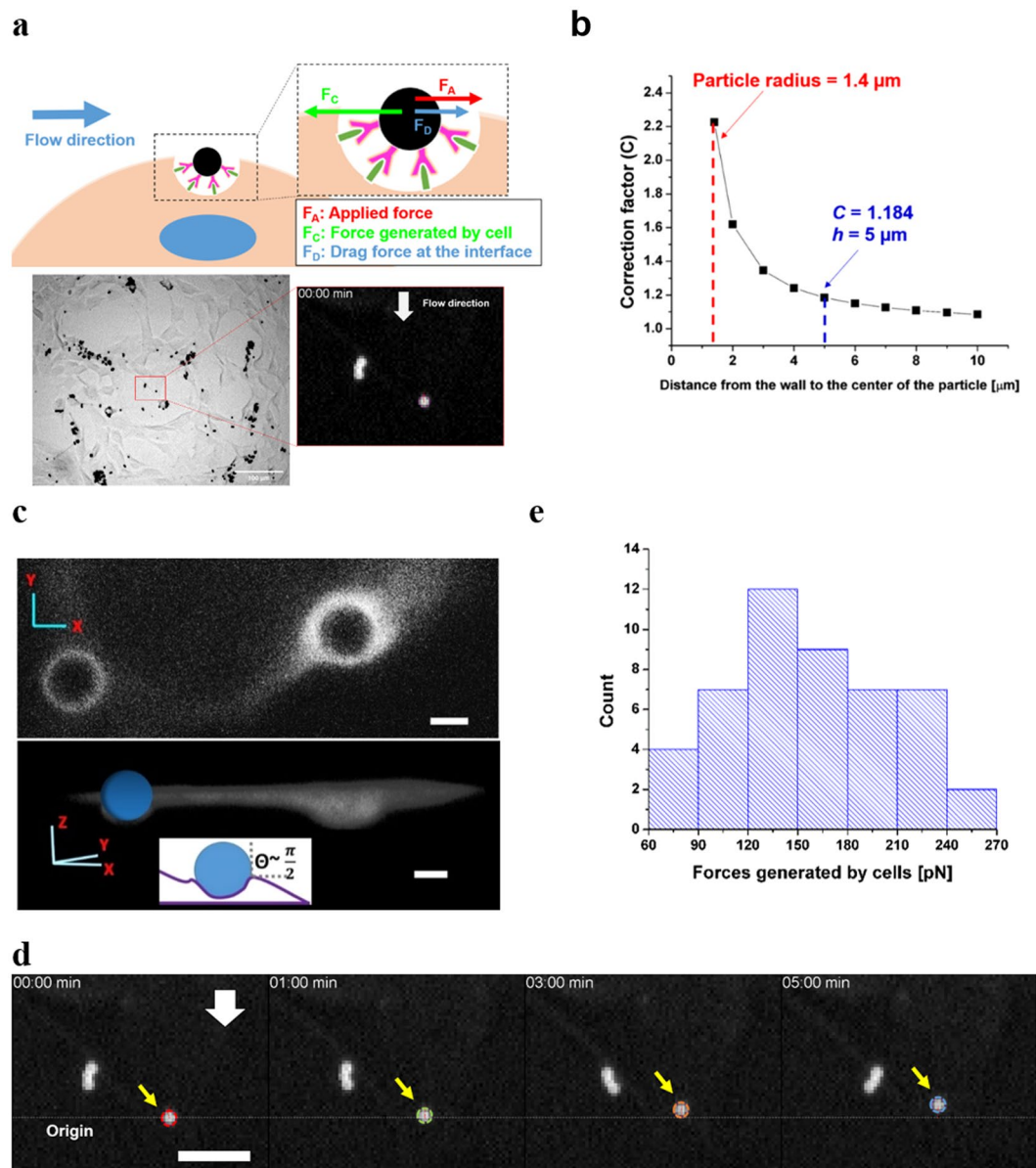


Figure 2. The traction forces on dorsal side of cells can be measured. **(a)** The dynamic displacement of the particle is driven by the forces generated by the cell to overcome the applied hydrodynamic force and drag force at the interface. In other words, the force generated by the cells is the vector sum of the applied hydrodynamic force and the drag force at the interface between the cell and the fluid. Please note that the original movies (Supplementary Movie S1) were inverted so that the particle appears to be bright and the background dark, for the purpose of better visualization. **(b)** The correction factor for the drag force near surfaces based on the computational simulation. **(c)** A representative x-y image (top) and 3D reconstruction image (bottom) show that the particles are around 50% enveloped by the cell membrane, forming 90° contact angle (inset) between the particle, the cell and medium. The membrane surrounding the particles appears to be brighter because the membrane is folded to accommodate the cell-bound particle. Scale bar: 2 μm. **(d)** A cell-bound particle is displaced when the flow is on at 10 μl/min and moves in the opposite direction to the flow. The flow was turned on 10 seconds before the timestamp 00:00 min. White arrow indicates flow direction. Scale bar: 20 μm. **(e)** 2.8-μm particles conjugated with CD80 on MDA-MB-231 cells were tracked, and the magnitude distribution of the force generated by the cells are shown in the histogram with average ± standard error of 157.6 pN ± 7.2 pN and median of 154.2 pN (n = 48).

$$C = \left[1 - \frac{9}{16} \left(\frac{d}{2h} \right) + \frac{1}{8} \left(\frac{d}{2h} \right)^3 - \frac{45}{256} \left(\frac{d}{2h} \right)^4 - \frac{1}{16} \left(\frac{d}{2h} \right)^5 \right]^{-1} \quad (3)$$

where d is the particle diameter and h is the distance between the particle centroid and the bottom surface (Fig. 2b). The height of the cell ranges from 3 μm to 8 μm^{44,45}. Because the variation in correction factor between

$h = 3 \mu\text{m}$ and $h = 8 \mu\text{m}$ is negligible (Fig. 2b), we adopted the universal value at $h = 5 \mu\text{m}$ for every estimation. The resulting C was 1.184. It should be noted that the shear stress or friction drag force due to the flow is negligible compared to the effect of pressure drag force exerted on to the particles in our system, given the size of the particles. The drag force (F_D) at the cell-fluid interface required to be overcome was calculated by the following equation characterizing particles moving at an interface⁴⁶, in this case between the medium and the cytoplasm

$$F_D = 6\pi a\mu_c u f \quad (4)$$

where f is the drag coefficient of a translating interfacial particle, and μ_c is the assumed viscosity of the protein network underneath the plasma membrane based on our measurement (550 Pa-s, see next section for details). The value of f is a function of the contact angle θ , described by the formula

$$f(\theta) = 0.5 \left[1 + \frac{9}{16} \cos \theta - 0.139 \cos^2 \theta \right] \quad (5)$$

The contact angle θ is defined as the angle between the horizontal line and the line tangent to the particle surface in contact of the cell/medium interface. The value of θ was determined by the 3D images of cells decorated with CD80-coated particles and stained with membrane dye (Fig. 2c). The particles exhibited $90^\circ \pm 5^\circ$ contact angle in the 10 particles examined using 63X magnification after fixing cells and staining them with the membrane dye. Given the variation in $f(\theta)$ was small ($<10^\circ$) and the resulting difference in the f value is negligible, $f(\theta)$ was calculated at $\theta = 90^\circ$ and used for all the estimation. Traction forces in 48 particles were calculated (Fig. 2d). The measured traction force magnitude was $157.6 \text{ pN} \pm 7.2 \text{ pN}$ (Fig. 2e, Supplementary Fig. S5). It should be noted that at the timescale of our measurement, the part of the cells in contact with the particles, namely the plasma membrane and the cortical actin network, can be viewed as a viscous fluid⁴⁷. Therefore, Eq. (4)⁴⁶, which corrects for particles moving at fluid interfaces, can be applied.

To compare our method to other force measurement methods, we also performed magnetic tweezers measurement to evaluate the dorsal traction forces transmitted via CTLA4-CD80 bonds, following the previously established protocol^{48–50}. The results obtained from the magnetic tweezers showed traction force values exerted through CTLA4-CD80 were of the same order of magnitudes with the results using our microfluidics-based method with no significant difference between the two measurement methods (Supplementary Fig. S6).

Next, we set to demonstrate our technique is suitable for measuring viscoelastic parameters of the cell. Two flow rates, $600 \mu\text{l}/\text{min}$ and $1000 \mu\text{l}/\text{min}$, were deployed, resulting in hydrodynamic forces of approximately 980 pN and 1.56 nN , which exceeded the cell-generated forces (Fig. 2e) by at least an order of magnitude. Interference by cell-generated forces during the measurement was thereby considered negligible. Upon flow application, anti-integrin antibody-coated particles were observed to be displaced in the flow direction (Supplementary Movie S2). Immediately after the flow was stopped, the particles moved back towards their initial positions (Fig. 3a). The dynamic displacement of the particles represented the responses of the cells to external mechanical perturbations. The displacement curve over time exhibits the typical response belonging to viscoelastic materials, consisting of a viscoelastic regime when a constant force is applied, and a recovery regime where the delayed elastic displacement and residual displacement were superimposed after the force was no longer applied (Fig. 3b). To determine the viscoelasticity of the cells, the displacement curves were fitted to the Kelvin-Voigt 4 element model (Supplementary Fig. S7), represented by two spring elements and two dashpot elements. The effective elastic moduli (E_0 and E_1) and the effective viscosity (μ_0 and μ_1) with relaxation time (τ) (Fig. 3c,d)⁵¹ can be determined by

$$J(t) = \frac{6\pi a X(t) C}{F_A} = \frac{1}{E_0} \left[1 - \frac{E_1}{E_0 + E_1} \exp\left(-\frac{t}{\tau_\sigma}\right) \right] + \frac{t}{\mu_0}, \quad \tau = \frac{\mu_1(E_0 + E_1)}{E_0 E_1} \quad (6)$$

$J(t)$ represents the compliance over time. The values of E_0 , E_1 , μ_0 , μ_1 and τ determined using the two flow rates were comparable without statistically significant differences. The results suggest our technique presents a suitable range of flow rates for viscoelasticity measurement in which the results are consistent. The average instant elastic modulus and standard error of $E_0 + E_1$ were $1.80 \text{ kPa} \pm 581 \text{ Pa}$ and $1.97 \text{ kPa} \pm 533 \text{ Pa}$ for $600 \mu\text{l}/\text{min}$ and $1000 \mu\text{l}/\text{min}$ respectively (Fig. 3e), agreeing with the previously reported measurement (Supplementary Table S2).

Acoustic force spectroscopy was recently developed^{52,53} for viscoelasticity measurement simultaneously in multiple cells, which can apply forces up to 500 pN if $6.84\text{-}\mu\text{m}$ particles are used. In this proof-of-concept report, we chose to use $2.8\text{-}\mu\text{m}$ particles, but our technique, with different choices of bead size, can provide broader range of forces from sub-pN to tens of nN. Passive microrheology, recording dynamic displacements of microparticles without external force perturbation, yields measurement results agreeing with the theoretical predictions in a wide range of biological context. However, passive microrheology requires correct assumption or prior knowledge of the fluids which the particles were immersed in. The rheological properties of the fluids can be controlled in our microfluidic-based method. In addition, passive microrheology requires high spatial resolution to obtain accurate measurement, given the displacement magnitude without external perturbation is subtle. Such requirement can only be fulfilled with microscopy of high magnification and high numerical aperture, which restricts the field of view and subsequently the throughput of the measurement⁵⁴. With the capacity to manipulate the flow rate and subsequent particle displacement using our method, high spatial resolution is a less instrumental restriction in many applications.

Next, we deployed a wide range of flow rates to demonstrate the capacity of determining the binding strength between ligands and receptors. Two binding pairs were tested: CD80 vs. CTLA4, and integrin vs. anti-integrin antibody. The particles were coated either by CD80 or anti-integrin antibody. The binding strength between CD80 and CTLA4 was tested in MDA-MB-231 cells, whereas the bond between integrin and anti-integrin was

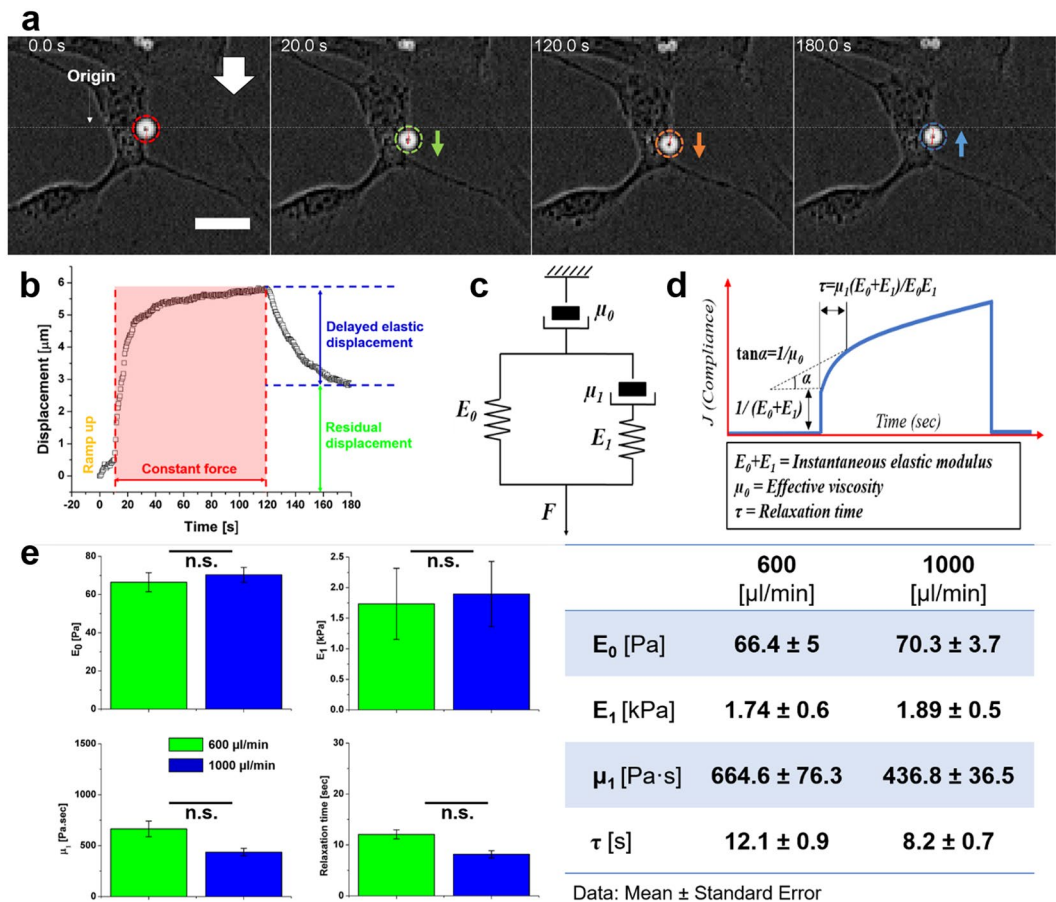


Figure 3. The viscoelasticity of single cells can be measured using flow rates of 600 and 1000 $\mu\text{l}/\text{min}$. (a) 2.8- μm particles conjugated with integrin are bound to the surface of the cells. A cell-bound particle is displaced when the flow is on and moves towards its initial position when the flow is off, exhibiting typical viscoelasticity. The original images were inverted so that the particle appears to be bright and the background dark, for the purpose of better visualization. White arrow indicates flow direction. Scale bar: 20 μm . (b) The particle displacement is plotted against time. (c,d) The typical viscoelastic behavior over time of the cell subjected to deforming forces can be observed in the plot. The Kelvin-Voigt 4 element model used to fit the displacement data consists of two spring elements and two dashpot elements representing the effective elastic modulus and the effective viscosity. (e) The viscoelastic parameters, including elastic moduli, E_0 and E_1 , viscosity μ_1 , and relaxation time τ , were evaluated by fitting the particle displacement under the flow rates of 600 $\mu\text{l}/\text{min}$ ($n = 53$) and 1000 $\mu\text{l}/\text{min}$ ($n = 80$). The values obtained from the two flow rates are comparable with no statistically significant differences. Bar (—): $p > 0.05$, n.s.: not significant.

tested in both MDA-MB-231 and osteosarcoma U2OS cells. Incremental flow rates were applied step-wise⁵⁵ with 30-second intervals for a duration of 270 seconds. The rate increment was 200 $\mu\text{l}/\text{min}$ per step (Fig. 4b). The number of cell-bound particles decreased as the flow rate increased (Fig. 4a and Supplementary Movie S3).

In the case of CD80-CTLA4 bond, a sharp drop in the number of cell-bound particles was observed when 320-pN hydrodynamic forces were applied (200 $\mu\text{l}/\text{min}$). The bond between integrin and anti-integrin antibody exhibited a distinct pattern (Fig. 4c) from CD80-CTLA4, but the pattern was consistent across cell types. The sharp reduction in cell-bound particles was detected at 640 pN (400 $\mu\text{l}/\text{min}$). However, the number of cell-bound particles did not further decrease even when higher forces were applied, indicating a sub-population of bonds between integrin and anti-integrin antibody exist, where the required rupture force is much higher than the maximal hydrodynamic forces in our platform. Notably, our observation agreed with the previous report by Sheetz and colleagues⁵⁶.

In this study, we present an economical, versatile and high-throughput force measurement technique. It should be noted that the accuracy of traction force estimation depends on the accuracy of the θ value (Fig. 2c). If θ ranges from $\pi/3$ to $2\pi/3$, the error can be as large as 33%. Therefore, measurement of θ by 3D imaging is recommended prior to calculation.

Our platform is not intended for single-molecule force measurement. Instead, the particles are coated with high-density ligands (5×10^7 ligands/particle), the rupture and traction forces measured are the products of *in situ* receptor density multiplied by force per molecule. By evaluating the contact area between the particle and the cell surface (Fig. 2c), the dorsal traction force generated per unit area can be estimated. Similarly, the force per unit

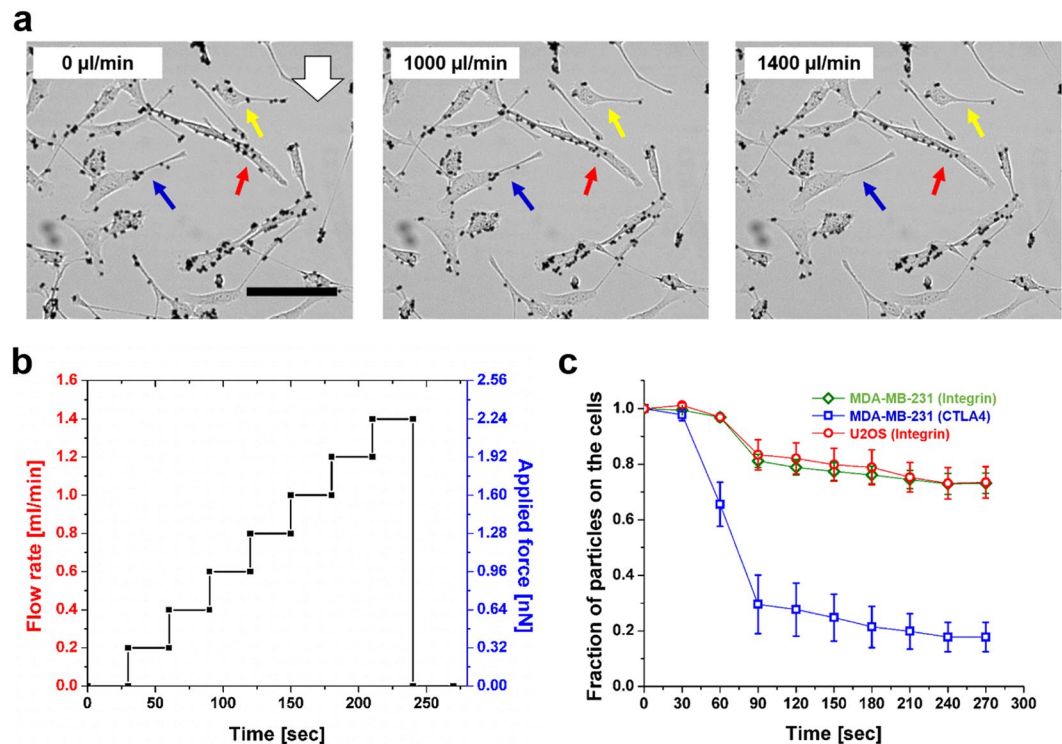


Figure 4. The rupture force between ligand-receptor bond can be measured *in situ* at the dorsal side of the cell using high flow rates. **(a)** Particles increasingly detach from the cells as the flow rate increases. For example, the ligand-receptor bond rupture can be observed in the cells indicated by the yellow, red, and blue arrows. White arrow indicates flow direction. Scale bar: 100 μm . **(b)** Particles bound to the cells are imaged over 270 seconds when subjected to incremental flow rates and the resulting applied forces. The flow rate was increased step-wise (step size = 200 $\mu\text{l}/\text{min}$, 30 seconds/step). **(c)** The number of cell-bound particles decreases as the flow rate and the resulting applied forces increase. The rupture forces of integrin-antibody bond and the CD80-CTLA4 bond are measured. The sharp drop of the particle number is observed in the case of CD80-CTLA4 at 200 $\mu\text{l}/\text{min}$, indicating approximately 320 pN of force is required to disrupt the bond formed between CD80 and CTLA4 at the cell surface. In the case of integrin-antibody, the measurement results from MDA-MB-231 and U2OS cells are consistent, where $\sim 27\%$ of the bond population are disengaged by forces of ~ 640 pN (400 $\mu\text{l}/\text{min}$).

area required to break two cells adherent to each other through specific ligand-receptor binding can be calculated. Our technique thereby is relevant in physiological scenarios and can be applied, for example, to evaluate forces required to disrupt cancer cell-endothelium association via ICAM-MUC1⁵⁷ bond before intrastation is initiated, or to evaluate the pulling force, transmitted through Notch and its ligands at the cell-cell interface during embryonic development⁵⁸.

Materials and Methods

Cell culture and reagents. The immortalized human breast carcinoma cell line MDA-MB-231 and human osteosarcoma cell line U2OS were maintained in culture medium (Dulbecco's Modified Eagle's Medium (ThermoFisher 11995073) for MDA-MB-231 and McCoy's 5A Medium (Sigma-Aldrich M8403) for U2OS. The media were supplemented with 100 U/mL penicillin and 100 $\mu\text{g}/\text{mL}$ streptomycin (1% v/v P/S) (ThermoFisher 15140122), and 10% (v/v) fetal bovine serum (ThermoFisher 26140079). The cells were cultured in 10 ml of supplemented culture medium in 10 cm diameter cell culture dish (Nest Scientific 704001) at 37 °C and 5% CO₂. Cells were collected using 0.25% trypsin and 2.21 mM EDTA (Corning Cellgro 25-053-CI).

Cell preparation in a microfluidic channel. Approximately 50,000 cells, with the density of 2,500,000 cells/ml, were seeded into a microfluidic channel (width (w) \times height (h) = 1 mm \times 100 μm) coated with Poly-L-lysine, Poly-D-lysine, fibronectin, and collagen (μ -Slide VI 0.1, Ibidi, 80666). The microfluidic device was placed in an incubator (5% CO₂ and 37 °C) for about 24 hours until cells adhered to the surface with a well-spread morphology.

Imaging and image processing. The time-lapse images were acquired using the optical microscope (Leica SP8) equipped with a CCD camera (Leica DFC365FX) and a 10X objective (NA 0.45). The frame rate of each time-lapse image series were set as indicated in each measurement procedure in the following. The 3D confocal images of particles on cells stained with membrane dye were performed using Leica SP8 with white light laser and photomultipliers. The z-sectioning of the 3D images was set at 0.01- μm intervals for 3D reconstruction based on

optimized 3D deconvolution using Hyugens Software (Scientific Volume Imaging). All images were processed and analyzed using FIJI-ImageJ (NIH) and MATLAB (R2018a, MathWorks).

Particle coating. To fabricate CD80- and anti-integrin $\alpha 5$ antibody-coated particles, we conjugated recombinant CD80-Fc (Biolegend 555404) or anti-integrin $\alpha 5$ antibody (Biolegend 328002) onto 2.8- μm Dynabeads (ThermoFischer 10003D) via Protein G. Dynabeads and CD80-Fc or anti-integrin $\alpha 5$ antibody, as mixed at the ratio of 1:5 (protein G: ligand). The mixture was incubated at room temperature while rotating at 30 rpm for 1 hour. The mixture was then washed for 3 times with PBS to exclude the free CD80 or anti-integrin $\alpha 5$ antibody in the buffer.

Membrane staining of the cells. Cells with CD80- or anti-integrin $\alpha 5$ antibody-coated particles bound to their surfaces were subject to the membrane dye staining to determine the interfacial contact angle between the cell and the medium as mentioned in the main text. The cells were incubated in the 1000X-diluted CellMaskTM plasma membrane dye (ThermoFischer C10046) in the appropriate medium at 37 °C for 5 minutes. The cells were then washed for 3 times with PBS before fixation by 4% paraformaldehyde. The fixed cells were then imaged using the Leica SP8 confocal microscope.

Microfluidic channel configurations for force measurement. CD80- and anti-integrin $\alpha 5$ antibody-coated particles were added into the microfluidic channel following the protocol provided by the manufacturer (Ibidi). After incubation for 5 minutes at 37 °C and 5% CO₂, the microfluidic channel was connected with a syringe pump (NE-1002X, Pump System Inc.), a syringe (60 mL, SMP Medical), silicone tubing (Ibidi 0841), and an elbow luer connector (Ibidi 10802). The channel was then mounted on the microscope.

Measurement of dorsal traction forces. A constant flow rate of 10 $\mu\text{l}/\text{min}$ resulting in 14 pN as the maximal particle drag force was utilized to create hydrodynamic forces. The MDA-MB-231 cells decorated with the CD80-coated particles were imaged at 10 s interval for 5 minutes. The particle coordinates were tracked to measure displacement using TrackMate (FIJI-ImageJ, NIH), and subsequently used to evaluate drag forces at the interface experienced by the particles. The drag force at the interface of the particle was calculated by the equation assuming the interfacial particle at the fluid-fluid interface as described in the main text⁵⁹. The dorsal traction force magnitudes were then calculated by adding the magnitudes of the applied force and the drag force at the interface. Five independent experiments were performed. Only non-aggregated single particles were selected for analysis.

Measurement of viscoelastic properties of the cell. We deployed two flow rates, 600 $\mu\text{l}/\text{min}$, and 1000 $\mu\text{l}/\text{min}$, to apply different forces on the anti-integrin-conjugated particles on MDA-MB-231 cells. The cells were imaged at 0.5 s interval for 3 minutes. The particle coordinates were tracked to measure displacement using TrackMate, and used for the assessment of the viscoelastic properties of the cells. Five independent experiments were performed. Only non-aggregated single particles were selected for analysis.

Measurement of the molecular bond strength. The step-wise flow rates ranging from 200 $\mu\text{l}/\text{min}$ to 1400 $\mu\text{l}/\text{min}$, with the 200 $\mu\text{l}/\text{min}$ increment, were applied to the channel to generate incremental forces exerted on the particles. Three groups, anti-integrin $\alpha 5$ antibody /integrin on MDA-MB-231 cells, anti-integrin $\alpha 5$ antibody /integrin on U2OS cells, and CD80/CTLA4 on MDA-MB-231 cells, were used for the measurement. The cells were imaged at 1 s interval for 4.5 minutes. The particle coordinates were tracked by TrackMate and used for the bond strength estimation. Three independent experiments were performed.

Estimation of the number of ligands conjugated to the particle. According to the data provided by the manufacturer, 1 mg of Dynabeads-protein G binds $\sim 8 \mu\text{g}$ of human IgG. Given that the density of the Dynabeads is $\sim 1.3 \text{ g}/\text{ml}$, 1 mg of Dynabeads equates to 6.09×10^8 particles. Given that the molecular weight of IgG is approximately 150 g/mole, 8 μg of IgG equates to 3.2×10^{16} molecules. Because we mixed the ligands and particles at the ratio of 1:5 (protein G: ligand), and protein G has high affinity to Fc-CD80 or IgG, resulting in saturation of the binding sites on the particle, it is estimated that each particle is conjugated with 5×10^7 ligands on its surface.

Measurement of traction forces using magnetic tweezers. The 2.8- μm , anti-CTLA4 paramagnetic particles were added to bind the surface of the cell. The 416-steel pole tip powered by Neodymium magnets (0.4-T surface field, K&J Magnets) was then positioned close to a paramagnetic particle bound to the cell. The particle motion induced by the magnetic field gradient was tracked over time. To calibrate the force field, unbound, free-moving particles in the image field were tracked. The magnetic forces were assumed equal to the drag forces experienced by the particle, which could be calculated by the modified Stokes equation. The dorsal traction was calculated based on the equation

$$F_C = F_M + F_D \quad (7)$$

where F_C , F_M , and F_D are the traction force generated by cell, applied magnetic force, and drag forces at the interface, respectively.

Numerical analyses of fluid flow and particle transport. We applied the finite element/volume method (FEM/FVM) to simulate fluid and particle dynamics available in ANSYS (version 14.5). The flow motion

can be described by solving two classical equations, conservation of mass and conservation of momentum (Navier-Stokes equation), with the assumption of steady-state and incompressible flow given by^{60,61}:

$$\nabla \cdot \mathbf{V} = 0 \quad (8)$$

$$-\nabla p + \mu \nabla^2 \mathbf{V} = \rho(\mathbf{V} \cdot \nabla) \mathbf{V} \quad (9)$$

where \mathbf{V} represents the fluid velocity vector and p the fluid pressure, μ the dynamic viscosity and ρ the water density.

Total 6 particles with 2.8- μm diameter were used in the simulation. The simulation was initiated by injecting particles into the inlet of the microfluidic channel with 1-mm width and 100- μm height. The particles were placed at varied locations in terms of distances to the bottom surface, ranging from 25 μm to 500 μm (Fig. S1). For the boundary conditions, constant flow rates of 10 $\mu\text{l}/\text{min}$, 50 $\mu\text{l}/\text{min}$, 100 $\mu\text{l}/\text{min}$, 300 $\mu\text{l}/\text{min}$, 600 $\mu\text{l}/\text{min}$, and 1000 $\mu\text{l}/\text{min}$, and the pressure of 0 Pa were set as the inlet and outlet conditions. The wall was assumed to be non-slip. The flow is laminar and Reynolds number ranges from 0.27 to 40 depending on the flow rate. For particle dynamics, particle transport equation was used⁶².

$$m \frac{d\mathbf{V}_p}{dt} = \frac{1}{8} \pi \rho_f d_p^2 C_D |\mathbf{V}_f - \mathbf{V}_p| (\mathbf{V}_f - \mathbf{V}_p) \quad (10)$$

where m , d_p , \mathbf{V}_p , ρ_f , C_D , and \mathbf{V}_f are the particle mass, particle diameter, particle velocity, fluid density, particle drag coefficient, and fluid velocity.

Drag coefficient, C_D , can be calculated using the Schiller-Naumann correlation as follows⁶³:

$$C_D = \frac{24}{Re_p} (1 + 0.15 Re_p^{0.687}) \quad (11)$$

where Re_p is the particle Reynolds number.

The hexahedral mesh was created using ANSYS ICEM-CFD. The number of elements and nodes were 140,679 and 150,000, respectively. The specialized program for simulation of fluid dynamics, ANSYS-CFX, was used for the computation. The root mean square (RMS) residuals were utilized to set convergence criteria as 10^{-4} – 10^{-5} ⁶⁴.

Calculation of the applied drag forces exerted on cells. The simulation showed that particles travel in the microfluidic channel in a smoothly continuous manner (Fig. S2). The traveling time and velocity of the particles were then quantified. It reveals that particles are slower when closer to the channel wall, due to the non-slip condition, resulting in longer traveling time near the wall compared to near the center (Fig. S3). Individual particle velocity is constant throughout the fully developed region of the channel. Particle drag forces were calculated using the modified Stokes equation as shown in Eq. (2)^{41,43}. The drag force decreases near the wall as it is proportional to the particle velocity (Fig. S4). The calculated drag force (squares in Fig. S4) for each flow rate was non-linearly fitted to the logistic model given by ($R^2 > 0.95$):

$$F = \frac{A_1 - A_2}{1 + (x/x_0)^p} + A_2 \quad (12)$$

The 4 parameters (A_1 , A_2 , x_0 , and p) acquired from the logistic model are shown in Table S1. To avoid the wall effects imposed by the side walls of the channel, only cells at locations more than 200 μm away from the side walls were analyzed.

Calculation of applied hydrodynamic forces exerted on particles. Given that the applied hydrodynamic force, or known as applied drag force, is a function of the distance from the wall/surface, the particle location was taken into account during the calculation. The hydrodynamic force can be computed by substituting the value of the distance into Eq. (13). To avoid the wall effects imposed by the side walls of the channel, only cells at locations more than 200 μm away from the side walls were analyzed.

Calculation of shear modulus, elastic modulus, and viscosity of the cell. After the dynamic displacement of each particle was determined, it was fit to the Kelvin-Voigt 4 element model⁵¹:

$$J(t) = \frac{6\pi a X(t) C}{F_A} = \frac{1}{G_0} \left[1 - \frac{G_1}{G_0 + G_1} \exp\left(-\frac{t}{\tau}\right) \right] + \frac{t}{\mu'_1}, \quad \tau = \frac{\mu'_1(G_0 + G_1)}{G_0 G_1} \quad (13)$$

where G_0 and G_1 are the shear modulus, and μ'_0 and μ'_1 are viscosity.

The calculated shear modulus and viscosity can be converted into the elastic modulus and the modified viscosity in the main text using the following form:

$$\begin{cases} E_i = 2G_i(1 + \nu) \\ \mu_i = 2\mu'_i(1 + \nu) \end{cases} \quad (14)$$

where the index, i , is 0 and 1. A Poisson ratio has been experimentally measured ranging from 0.4 to 0.5⁶⁵. Here we used 0.4 as the Poisson ratio. To avoid the wall effects imposed by the side walls of the channel, only cells at locations more than 200 μm away from the side walls were analyzed.

Statistical analysis. The data in this study were statistically analyzed using the Student's t -test for paired data (two-tail). P values less than 0.05 were taken into account statistically significant. Data are presented as mean \pm standard error.

References

- Polacheck, W. J. & Chen, C. S. Measuring cell-generated forces: a guide to the available tools. *Nat. Methods* **13**, 415–423 (2016).
- Discher, D. E., Janmey, P. & Wang, Y. L. Tissue Cells Feel and Respond to the Stiffness of Their Substrate. *Science (80-)* **310**, 1139–1143 (2005).
- Hoffman, B. D. & Crocker, J. C. Cell Mechanics: Dissecting the Physical Responses of Cells to Force. *Annu. Rev. Biomed. Eng.* **11**, 259–288 (2009).
- Kuo, S. & Sheetz, M. Force of single kinesin molecules measured with optical tweezers. *Science (80-)*. **260**, 232–234 (1993).
- Capitanio, M. & Pavone, F. S. Interrogating biology with force: Single molecule high-resolution measurements with optical tweezers. *Biophysical Journal* **105**, 1293–1303 (2013).
- Issac, A., Partha Sarathi, M. & Dutta, M. K. An adaptive threshold based image processing technique for improved glaucoma detection and classification. *Comput. Methods Programs Biomed.* **122**, 229–244 (2015).
- Müller, D. J., Helenius, J., Alsteens, D. & Dufrene, Y. F. Force probing surfaces of living cells to molecular resolution. *Nature Chemical Biology* **5**, 383–390 (2009).
- Blakely, B. L. *et al.* A DNA-based molecular probe for optically reporting cellular traction forces. *Nat. Methods* **11**, 1229–1232 (2014).
- Wang, X. & Ha, T. Defining Single Molecular Forces Required to Activate Integrin and Notch Signaling. *Science (80-)*. **340**, 991–994 (2013).
- Zhang, Y., Ge, C., Zhu, C. & Salaita, K. DNA-based digital tension probes reveal integrin forces during early cell adhesion. *Nat. Commun.* **5**, 5167 (2014).
- Sabass, B., Gardel, M. L., Waterman, C. M. & Schwarz, U. S. High resolution traction force microscopy based on experimental and computational advances. *Biophys. J.* **94**, 207–20 (2008).
- Han, S. J., Oak, Y., Groisman, A. & Danuser, G. Traction microscopy to identify force modulation in subresolution adhesions. *Nat. Methods* **12**, 653–6 (2015).
- Liu, Z. *et al.* Mechanical tugging force regulates the size of cell-cell junctions. *Proc. Natl. Acad. Sci.* **107**, 9944–9949 (2010).
- Schoen, I., Hu, W., Klotzsch, E. & Vogel, V. Probing Cellular Traction Forces by Micropillar Arrays: Contribution of Substrate Warping to Pillar Deflection. *Nano Lett.* **10**, 1823–1830 (2010).
- Swaminathan, V. *et al.* Mechanical Stiffness grades metastatic potential in patient tumor cells and in cancer cell lines. *Cancer Res.* **71**, 5075–5080 (2011).
- Bausch, A. R., Ziemann, F., Boulbitch, A. A., Jacobson, K. & Sackmann, E. Local measurements of viscoelastic parameters of adherent cell surfaces by magnetic bead microrheometry. *Biophys. J.* **75**, 2038–2049 (1998).
- Sawicka, A. *et al.* Micropipette force probe to quantify single-cell force generation: application to T-cell activation. *Mol. Biol. Cell* **28**, 3229–3239 (2017).
- Basu, R. *et al.* Cytotoxic T Cells Use Mechanical Force to Potentiate Target Cell Killing. *Cell* **165**, 100–110 (2016).
- Maruthamuthu, V., Sabass, B., Schwarz, U. S. & Gardel, M. L. Cell-ECM traction force modulates endogenous tension at cell-cell contacts. *Proc. Natl. Acad. Sci.* **108**, 4708–4713 (2011).
- Fu, J. *et al.* Mechanical regulation of cell function with geometrically modulated elastomeric substrates. *Nat. Methods* **7**, 733–736 (2010).
- Galbraith, C. G. & Sheetz, M. P. Keratocytes Pull with Similar Forces on Their Dorsal and Ventral Surfaces. *J. Cell Biol.* **147**, 1313–1324 (1999).
- Friedl, P., Locker, J., Sahai, E. & Segall, J. E. Classifying collective cancer cell invasion. *Nat. Cell Biol.* **14**, 777–783 (2012).
- Breckenridge, M. T., Egelhoff, T. T. & Baskaran, H. A microfluidic imaging chamber for the direct observation of chemotactic transmigration. *Biomed. Microdevices* **12**, 543–553 (2010).
- Przybyla, L., Lakins, J. N., Sunyer, R., Treppe, X. & Weaver, V. M. Monitoring developmental force distributions in reconstituted embryonic epithelia. *Methods* **94**, 101–113 (2016).
- Yamada, S., Iino, T., Bessho, Y., Hosokawa, Y. & Matsui, T. Quantitative analysis of mechanical force required for cell extrusion in zebrafish embryonic epithelia. *Biol. Open* **6**, 1575–1580 (2017).
- Campàs, O. A toolbox to explore the mechanics of living embryonic tissues. *Semin. Cell Dev. Biol.* **55**, 119–30 (2016).
- Hui, K. L., Balagopalan, L., Samelson, L. E. & Upadhyaya, A. Cytoskeletal forces during signaling activation in Jurkat T-cells. *Mol. Biol. Cell* **26**, 685–95 (2015).
- Hou, T. Z. *et al.* A Transendocytosis Model of CTLA-4 Function Predicts Its Suppressive Behavior on Regulatory T Cells. *J. Immunol.* **194**, 2148–2159 (2015).
- Walker, L. S. K. & Sansom, D. M. The emerging role of CTLA4 as a cell-extrinsic regulator of T cell responses. *Nat. Rev. Immunol.* **11**, 852–63 (2011).
- Egen, J. G. & Allison, J. P. Cytotoxic T Lymphocyte Antigen-4 Accumulation in the Immunological Synapse Is Regulated by TCR Signal Strength. *Immunity* **16**, 23–35 (2002).
- Yu, H. *et al.* Cytotoxic T lymphocyte antigen 4 expression in human breast cancer: implications for prognosis. *Cancer Immunol. Immunother.* **64**, 853–60 (2015).
- Phan, G. Q. *et al.* Cancer regression and autoimmunity induced by cytotoxic T lymphocyte-associated antigen 4 blockade in patients with metastatic melanoma. *Proc. Natl. Acad. Sci.* **100**, 8372–8377 (2003).
- Ruocco, M. G. *et al.* Suppressing T cell motility induced by anti-CTLA-4 monotherapy improves antitumor effects. *J. Clin. Invest.* **122**, 3718–30 (2012).
- McCoy, K. D. & Le Gros, G. The role of CTLA-4 in the regulation of T cell immune responses. *Immunol. Cell Biol.* **77**, 1–10 (1999).
- Walker, L. S. K. Treg and CTLA-4: two intertwining pathways to immune tolerance. *J. Autoimmun.* **45**, 49–57 (2013).
- Tai, X. *et al.* Basis of CTLA-4 function in regulatory and conventional CD4+ T cells. *Blood* **119**, 5155–5163 (2012).
- Contardi, E. *et al.* CTLA-4 is constitutively expressed on tumor cells and can trigger apoptosis upon ligand interaction. *Int. J. Cancer* **117**, 538–550 (2005).
- Marshall, B. T. *et al.* Direct observation of catch bonds involving cell-adhesion molecules. *Nature* **423**, 190–193 (2003).
- Zhu, C. *et al.* Platelet glycoprotein Iba forms catch bonds with human WT vWF but not with type 2B von Willebrand disease vWF. *J. Clin. Invest.* **118**, 3195–3207 (2008).
- Bangasser, B. L., Rosenfeld, S. S. & Odde, D. J. Determinants of Maximal Force Transmission in a Motor-Clutch Model of Cell Traction in a Compliant Microenvironment. *Biophys. J.* **105**, 581–592 (2013).
- Hensley, Z. D. & Papavassiliou, D. V. Drag coefficient correction for spherical and nonspherical particles suspended in square microducts. *Ind. Eng. Chem. Res.* **53**, 10465–10474 (2014).

42. Kirby, B. J. *Micro- and Nanoscale Fluid Mechanics, Transport in Microfluidic Devices*. Cambridge University Press (2010).
43. Schäffet, E., Nørrelykke, S. F. & Howard, J. Surface forces and drag coefficients of microspheres near a plane surface measured with optical tweezers. *Langmuir* **23**, 3654–3665 (2007).
44. Vaughan, T. J., Haugh, M. G. & McNamara, L. M. A fluid-structure interaction model to characterize bone cell stimulation in parallel-plate flow chamber systems. *J. R. Soc. Interface* **10**, 20120900–20120900 (2013).
45. Ernst, O., Lieske, A., Jäger, M., Lankenau, A. & Duschl, C. Control of cell detachment in a microfluidic device using a thermo-responsive copolymer on a gold substrate. *Lab Chip* **7**, 1322 (2007).
46. Dörr, A., Hardt, S., Masoud, H. & Stone, H. A. Drag and diffusion coefficients of a spherical particle attached to a fluid–fluid interface. *J. Fluid Mech.* **790**, 607–618 (2016).
47. Mogilner, A. & Manhart, A. Intracellular Fluid Mechanics: Coupling Cytoplasmic Flow with Active Cytoskeletal Gel. *Annu. Rev. Fluid Mech.* **50**, 347–370 (2017).
48. Park, S. *et al.* Mechanical Characterization of hiPSC-Derived Cardiac Tissues for Quality Control. *Adv. Biosyst.* **2**, 1800251 (2018).
49. Pittman, M. & Chen, Y. 3D-printed magnetic tweezers for dorsal traction force measurement. *Biotechniques* **65**, 347–349 (2018).
50. Bush, J. & Maruthamuthu, V. *In situ* determination of exerted forces in magnetic pulling cytometry. *ALP Adv.* **9**, 035221 (2019).
51. Bausch, A. R., Möller, W. & Sackmann, E. Measurement of Local Viscoelasticity and Forces in Living Cells by Magnetic Tweezers. *Biophys. J.* **76**, 573–579 (1999).
52. Sorkin, R. *et al.* Probing cellular mechanics with acoustic force spectroscopy. *Mol. Biol. Cell*, <https://doi.org/10.1091/mbc.e18-03-0154> (2018).
53. Kamsma, D., Creighton, R., Sitters, G., Wuite, G. J. L. & Peterman, E. J. G. Tuning the Music: Acoustic Force Spectroscopy (AFS) 2.0. *Methods* **105**, 26–33 (2016).
54. Wirtz, D. Particle-Tracking Microrheology of Living Cells: Principles and Applications. *Annu. Rev. Biophys.* **38**, 301–326 (2009).
55. Lu, H. *et al.* Microfluidic shear devices for quantitative analysis of cell adhesion. *Anal. Chem.* **76**, 5257–5264 (2004).
56. Nishizaka, T., Shi, Q. & Sheetz, M. P. Position-dependent linkages of fibronectin- integrin-cytoskeleton. *Proc. Natl. Acad. Sci.* **97**, 692–697 (2000).
57. Reymond, N., d’Água, B. B. & Ridley, A. J. Crossing the endothelial barrier during metastasis. *Nat. Rev. Cancer* **13**, 858–870 (2013).
58. Meloty-Kapella, L., Shergill, B., Kuon, J., Botvinick, E. & Weinmaster, G. Notch Ligand Endocytosis Generates Mechanical Pulling Force Dependent on Dynamin, Epsins, and Actin. *Dev. Cell* **22**, 1299–1312 (2012).
59. Aaron, D. & Hardt, S. Drag and diffusion coefficients of a spherical particle attached to a fluid interface. *J. Fluid Mech.* 1–11, <https://doi.org/10.1017/jfm.2016.41> (2015).
60. Stylianopoulos, T. *et al.* Permeability calculations in three-dimensional isotropic and oriented fiber networks. *Phys. Fluids* **20** (2008).
61. Park, S. M., Min, Y. U., Kang, M. J., Kim, K. C. & Ji, H. S. *In Vitro* Hemodynamic Study On The Stenotic Right Coronary Artery Using Experimental And Numerical Analysis. *J. Mech. Med. Biol.* **10**, 695–712 (2010).
62. Park, S., Whittington, C., Voytik-Harbin, S. L. & Han, B. Microstructural Parameter-Based Modeling for Transport Properties of Collagen Matrices. *J. Biomech. Eng.* **137**, 061003 (2015).
63. Mirabolghasemi, M., Prodanović, M., DiCarlo, D. & Ji, H. Prediction of empirical properties using direct pore-scale simulation of straining through 3D microtomography images of porous media. *J. Hydrol.* **529**, 768–778 (2015).
64. Park, S. Computational modeling for prediction of the shear stress of three-dimensional isotropic and aligned fiber networks. *Comput. Methods Programs Biomed.* **148**, 91–98 (2017).
65. Mahaffy, R., Park, S., Gerde, E., Kas, J. & Shih, C. Quantitative Analysis of the Viscoelastic Properties of Thin Regions of Fibroblasts Using Atomic Force Microscopy. *Biophys. J.* **86**, 1777–1793 (2004).

Author Contributions

S.P. and Y.C. formulated the concepts and designed the experiments. S.P., Y.J. and Y.C. performed the experiments. S.P. and Y.J. performed the data analysis. S.P. and Y.C. wrote the manuscript. S.P. performed the simulation.

Additional Information

Supplementary information accompanies this paper at <https://doi.org/10.1038/s41598-019-49592-1>.

Competing Interests: The authors declare no competing interests.

Publisher’s note Springer Nature remains neutral with regard to jurisdictional claims in published maps and institutional affiliations.



Open Access This article is licensed under a Creative Commons Attribution 4.0 International License, which permits use, sharing, adaptation, distribution and reproduction in any medium or format, as long as you give appropriate credit to the original author(s) and the source, provide a link to the Creative Commons license, and indicate if changes were made. The images or other third party material in this article are included in the article’s Creative Commons license, unless indicated otherwise in a credit line to the material. If material is not included in the article’s Creative Commons license and your intended use is not permitted by statutory regulation or exceeds the permitted use, you will need to obtain permission directly from the copyright holder. To view a copy of this license, visit <http://creativecommons.org/licenses/by/4.0/>.

© The Author(s) 2019